

# Red Supergiant Stars within the Local Group

Lee. R. Patrick



Doctor of Philosophy  
The University of Edinburgh  
March 2016

# **Chapter 1**

## **First steps outside the Local Group of Galaxies. Red Supergiants in NGC 55**

### **1.1 Opening Remarks**

To improve the quality of the data reduction I enlisted the help of a fellow student, Owen Turner, who has provided some additional corrections to the standard KMOS/esorex pipeline to correct for the readout bias and to improve the pipeline's bad pixel map. Details of this procedure are given in the text and the reader is referred to Turner et al. (in prep) for a more in depth discussion of the steps taken.

### **1.2 Introduction**

NGC 55 is a galaxy located outside of the Local Group of Galaxies within the Sculptor Group at a distance of  $1.94 \pm 0.03$  Mpc (Pietrzyński et al., 2006; Gieren et al., 2008) which, before the emergence of the Araucaria Project (Gieren et al., 2005), had been subject to considerable uncertainty (e.g. Pritchett et al., 1987; van de Steene et al., 2006).

The Sculptor Group is considered to be the closest group of galaxies to our

own and offers a fantastic laboratory with which to test theories of stellar and galactic evolution. Using an 8-m class telescope, one can resolve individual stars within this group. Association to the Sculptor group however, is a contentious issue. Distance estimates vary to each galaxy, but typically when one references this group the main galaxies associated to this reference are: NGC 55, NGC 247, NGC 253, NGC 300 and NGC 7793. Where NGC 253 is a large starburst galaxy which is the brightest and most dominant galaxy within this group. In addition to these five large spiral galaxies, there are also numerous ( $\sim 20$ ) dwarf galaxies associated to this group.

By revising distances for nine of these dwarfs Karachentsev et al. (2003) postulated that the Sculptor group was actually more like a filament of galaxies, which intersects the Milky Way group, where NGC 55 and NGC 300 and their surrounding satellite galaxies were potentially not associated with the main group of galaxies in this filament. Regardless of the geometry and association to the Sculptor Group, NGC 55 is the nearest large galaxy to the MW group in the direction of the Sculptor Group.

The morphology of NGC 55 is asymmetric and complicated owing to the high inclination angle (up to  $80^\circ$ ; Hummel, Dettmar & Wielebinski, 1986; Westmeier, Koribalski & Braun, 2013). de Vaucouleurs (1961) classified this galaxy as an LMC-like spiral barred galaxy (SB(s)m) where the bar is seen along the line of sight de Vaucouleurs (1961) prompting various claims that this galaxy is an edge-on analogue of the LMC (e.g. Robinson & van Damme, 1964, although not cited heavily – two citations in 50 years – the idea propagated). Figure 1.1 shows NGC 55 and its complicated morphology where one can see the edge-on disk along the major axis of the galaxy and the brighter central part of the galaxy represents the head of the bar. In addition, to NGC 55 being orientated nearly edge on, extending from the disk-bar system there exists many star formation features such as giant H II regions as well as supergiant filaments and shells which are thought to allow ionising radiation to be transported to the halo where star-formation is currently occurring (Ferguson, Wyse & Gallagher, 1996).

The morphology of NGC 55, as well as its known population of massive hot stars (Castro et al., 2008, 2012), points to a recent history of intense star formation. This is supported by the infrared morphology of NGC 55 which is dominated by young star-forming features (Engelbracht et al., 2004, with a star formation rate of  $0.22 \text{ M}_\odot \text{yr}^{-1}$ ) as well as indications from near-IR imaging (Davidge, 2005).



**Figure 1.1** Image of NGC 55 where the edge disk of the galaxy makes up the major axis and the bright central region represents the head of the bar containing intense star-forming regions. Image from the Wide Field Imager on the 2.2-metre MPG/ESO telescope at ESO La Silla Observatory. Credit: ESO, press release.

The metal content of NGC 55 is expected to be LMC-like, which is supported by Castro et al. (2012) who measured metallicities of 12 blue supergiants using optical spectroscopy and found a mean metallicity  $[Z] = -0.40 \pm 0.13$  dex. In addition, Webster & Smith (1983) measure abundances of seven H II regions across the disk of NGC 55 using the strong-line method (as well as four measurements of the auroral “direct” line method) and found a similar LMC-like metallicity.

Even though the hot massive star population of NGC 55 has been explored, there currently exists no confirmed RSGs in NGC 55, although Davidge (2005) note that the near-IR CMDs of fields within the disk of NGC 55 reveal signatures of RSGs. This study represents the first quantitative study of RSGs in NGC 55 and, by measuring metallicities of this population, will provide a crucial test of the metallicity gradient within this galaxy.

In this chapter I describe the observations undertaken in Section 1.3 and highlight the target selection method and its uncertainties. Section ?? details the data reduction process and its complications owing to the poor S/N ratios of the observations. I then present the main results of the chapter in Section 1.5 where I first measure radial velocities for each epoch of the RGSs, confirming their

membership NGC 55, and then go on to measure stellar parameters for each target using the *J*-band analysis technique described in detail in Chapter ???. Section ?? presents a discussion of the results and the main conclusions are presented in Section 1.6.

## 1.3 Observations

### 1.3.1 Target Selection

Targets were selected based on the optical photometry from the ACS Nearby Galaxy Survey Treasury (blue; ANGST Dalcanton et al., 2009) project. The optical CMD which is used to select targets is displayed in Figure 1.3, where the RSG candidates are within the black box and the observed targets are highlighted in red. This method of target selection is preferred as a result of the limited extent of near-IR photometry in this area. The ANGST project publicly available photometry for several fields within the disk of NGC 55 that are displayed as small white squares in Figure 1.2, overlaid on a DSS image. In addition to the ANGST HST photometry, ground-based optical photometry is obtained from the Araucaria Project which covers the full spatial extent of NGC 55 (large white rectangles in Figure 1.2).

The selection criteria used in this study makes is based optical  $F606 - F814$  colours and  $F814$  magnitudes. Owing to their cool temperatures and extreme luminosities RSGs are known to exist in a “plume” at the tip of a structure of cool stars in the  $F606 - F814$ ,  $F814$  CMD (e.g. Gazak et al., 2015). Figure 1.3 displays this CMD and the region of parameter space where RSG candidates reside is marked with a grey box. This box has the limits  $17 < F814 < 19$  and  $1.2 < F606 - F814 < 3.5$  following Gazak et al. (2015), where the faint magnitude limit is chosen to select only targets which will have a  $S/N = 100$  in the original observing proposal. As with selection criteria in the near-IR, the lower limit of this criteria is contaminated with a population of super-AGB stars which can have luminosities comparable to the faintest RSGs (e.g. Nikolaev & Weinberg, 2000). However, as stated in Chapter ?? these stars are known to have lifetimes similar to the lowest mass RSGs and arguably still trace the young stellar population of this galaxy.

Table 1.1 shows ground- and space-based optical photometry of the KMOS targets

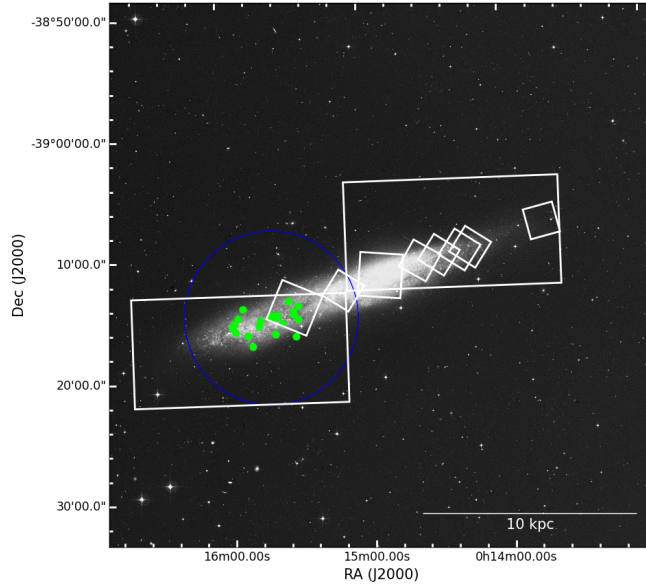


**Figure 1.2** DSS image of NGC 55 with KMOS targets overlaid in green and photometric footprints from the Araucaria Project (Gieren et al., 2005) in white rectangles and the ANGST project (Dalcanton et al., 2009) in the smaller white squares.

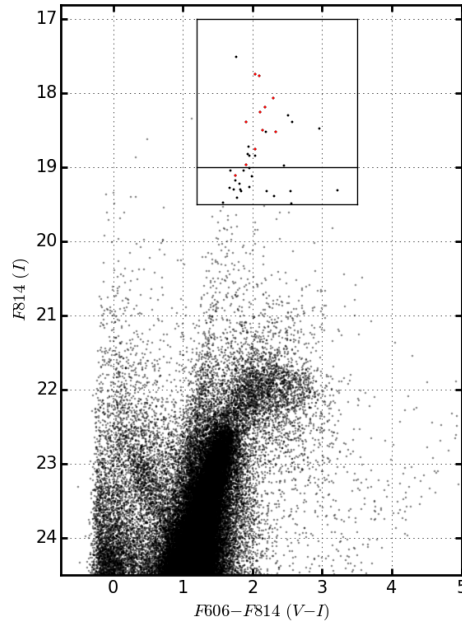


**Figure 1.3** NGC 55  $V - I$  colour-magnitude diagram from the ACS Nearby Galaxy Survey Treasury (ANGST Dalcanton et al., 2009) project. The black box defines the selection criteria for candidate RSGs, which is defined as  $17 < F814 < 19$  and  $1.2 < F606 - F814 < 3.5$ . The lower-panel of the black box defines priority 2 RSG candidates.

along with their radial velocities which confirm many of these targets as NGC 55 RSGs (see Section 1.5.1).

## 1.4 Observations and Data Reduction

These observations are part of the the KMOS guaranteed time observations (GTO) [SO ID: 092.B-0088(A)] that [proposed to measure spatial variations in metallicities NGC 55 and NGC 300 both at  $d = 1$  pc. This included three pointings in NGC 55 containing  $\sim 60$  RSG candidates. However, during the observations in October 2013, as a result of poor conditions, only half the requested time on one field in NGC 55 was observed. In order to supplement this partially completed [proposal], the proposal was re-submitted as a back-up OB for subsequent GTO.

As back-up observations, this [was observed on two nights in August 2014. Therefore, this [was observed on four different nights: 14-10-2013, 16-10-2013, 14-09-2014 and 15-10-2014 as detailed by Table 1.2. The observations on each night consisted of science exposures (O) with sky offset exposures (S) interveaved in an O, S, O observing pattern, where each exposure is 600 s.

In addition [on each night a standard set of KMOS calibration files was obtained as well as standard star observations on each night. In October 2013 HIP 3820 (B8 V; Houk, 1978) was observed using the 24-arm telluric template (KMOS\_spec\_acq\_stdstarscipatt). However, on 14-10-2013, this OB was interrupted and several of the IFUs (particularly on detector two) were not observed with the 24-arm recipe: this OB was not repeated.

In August 2014 the 3-arm telluric template (KMOS\_spec\_cal\_stdstar) was observed as opposed to the full 24-arm template. However, on both of these nights both HIP 3820 and HIP 18926 (B3 V; Houk & Smith-Moore, 1988) were observed as a standard star.

The quality of the observations taken on each night varies significantly. The first set of observations (14-09-2013) were taken in excellent conditions where the seeing conditions were stable with good transparency. As one would expect with back-up observations the conditions were not so [sic]. On both nights where this [was observed as a back-up target, the conditions were varying significantly throughout the night with patchy, sometimes significant, cloud coverage.

**Table 1.1** Summary of *VLT-KMOS* targets in *NGC 55*.

ID	$\alpha$ (J2000)	$\delta$ (J2000)	$V^a$	$I^a$	$F^b$	$rv$ (km s $^{-1}$ )			$\langle rv \rangle$ (km s $^{-1}$ )	Notes
						14-09-2013	16-10-2013	14-09-2014		
NGC55-RSG19	xx	00:15:29.190	-39:14:08.20	19.914	17.731	19.85	17.76	205 $\pm$ 4	178 $\pm$ 7	191 $\pm$ 7
NGC55-RSG20	xx	00:15:29.520	-39:15:13.00	20.832	18.952	20.86	19.11	194 $\pm$ 14	220 $\pm$ 5	-
NGC55-RSG22	xx	00:15:30.520	-39:16:36.70	20.406	18.589	-	95 $\pm$ 14	-41 $\pm$ 26	-	-
NGC55-RSG24	xx	00:15:31.460	-39:14:46.30	20.612	18.475	20.29	18.38	186 $\pm$ 6	194 $\pm$ 7	192 $\pm$ 16
NGC55-RSG25	xx	00:15:31.490	-39:14:32.40	20.316	18.394	20.63	18.49	204 $\pm$ 12	217 $\pm$ 16	200 $\pm$ 26
NGC55-RSG26	xx	00:15:33.160	-39:13:42.00	20.572	17.964	20.35	18.06	174 $\pm$ 9	173 $\pm$ 8	173 $\pm$ 1
NGC55-RSG28	xx	00:15:36.160	-39:15:29.40	21.001	18.892	20.87	18.97	233 $\pm$ 17	161 $\pm$ 20	-
NGC55-RSG30	xx	00:15:38.030	-39:14:50.20	20.867	18.730	20.79	18.75	212 $\pm$ 10	215 $\pm$ 10	203 $\pm$ 41
NGC55-RSG35	xx	00:15:39.260	-39:15:01.70	20.007	17.872	19.78	17.73	202 $\pm$ 3	206 $\pm$ 4	212 $\pm$ 22
NGC55-RSG36	xx	00:15:39.520	-39:16:23.10	19.915	18.462	-	-188 $\pm$ 31	-284 $\pm$ 16	-588 $\pm$ 35	213 $\pm$ 2
NGC55-RSG39	xx	00:15:40.260	-39:15:01.00	19.654	17.970	20.36	18.19	206 $\pm$ 11	192 $\pm$ 5	-
NGC55-RSG43	xx	00:15:40.700	-39:14:50.20	19.957	18.183	20.36	18.25	-220 $\pm$ 20 <sup>c</sup>	196 $\pm$ 5	193 $\pm$ 14
NGC55-RSG46	xx	00:15:41.640	-39:14:58.80	21.591	18.441	20.85	18.52	228 $\pm$ 5	195 $\pm$ 6	204 $\pm$ 5
NGC55-RSG57	xx	00:15:45.590	-39:15:16.40	20.010	18.220	-	-	217 $\pm$ 10	197 $\pm$ 6	-
NGC55-RSG58	xx	00:15:46.270	-39:15:43.20	20.619	18.400	-	-	236 $\pm$ 8	216 $\pm$ 3	218 $\pm$ 8
NGC55-RSG60	xx	00:15:49.180	-39:17:19.80	21.393	18.847	-	-	-73 $\pm$ 39	26 $\pm$ 26	-
NGC55-RSG65	xx	00:15:51.250	-39:16:26.40	19.706	17.653	-	-	224 $\pm$ 5	215 $\pm$ 4	218 $\pm$ 8
NGC55-RSG67	xx	00:15:53.110	-39:14:13.60	19.925	18.047	-	-	25 $\pm$ 24 <sup>c</sup>	6 $\pm$ 31 <sup>c</sup>	193 $\pm$ 16
NGC55-RSG69	xx	00:15:55.280	-39:15:00.10	20.470	18.666	-	-	231 $\pm$ 5	195 $\pm$ 9	222 $\pm$ 18
NGC55-RSG70	xx	00:15:56.310	-39:16:08.60	22.300	18.907	-	-	155 $\pm$ 12	187 $\pm$ 9	180 $\pm$ 20
NGC55-RSG71	xx	00:15:56.900	-39:15:27.50	20.401	18.559	-	-	197 $\pm$ 11	214 $\pm$ 11	206 $\pm$ 12
NGC55-RSG73	xx	00:15:57.710	-39:15:41.50	20.489	18.411	-	-	161 $\pm$ 7 <sup>b</sup>	178 $\pm$ 6	171 $\pm$ 11

<sup>a</sup> Ground based data from the Araucaria Project Pietrzynski et al. (2006), with typical photometric uncertainty 0.075 and 0.016 in *V* and *I* bands respectively.

<sup>b</sup> HST ANGST photometry from Dalcanton et al. (2009), with typical errors 0.12, 0.13 in *F606* and *F814* bands respectively.

<sup>c</sup> Value excluded from average for target.

**Table 1.2** *NGC 55 observing log*

Date	Seeing Conditions ( <i>arcsec</i> )	Airmass	Number of Exposures	Notes
14-10-2013	0''.8–1''.2	1.0–1.8	6 × 600s	Observed by author
16-10-2013	0''.8–1''.2	1.0–1.3	14 × 600s	Observed by author
14-09-2014	0''.4–2''.2	1.0–1.9	24 × 600s	Back-up observations
15-09-2014	1''.1–1''.6	1.1–1.5	12 × 600s	Back-up observations

**Table 1.3** *Measured velocity resolution and resolving power across each detector.*

Date	Det.	IFUs	Ne $\lambda 1.17700 \mu\text{m}$		Ar $\lambda 1.21430 \mu\text{m}$	
			FWHM (km s $^{-1}$ )	R	FWHM (km s $^{-1}$ )	R
14-10-2013	1	1-8	95.48 ± 2.42	3140 ± 80	90.71 ± 2.09	3305 ± 76
	2	9-16	88.67 ± 1.67	3381 ± 64	86.35 ± 1.84	3472 ± 74
	3	17-24	82.89 ± 1.81	3617 ± 79	80.56 ± 2.11	3721 ± 97
16-10-2013	1	1-8	95.48 ± 2.46	3140 ± 81	90.78 ± 2.12	3302 ± 77
	2	9-16	88.91 ± 1.66	3371 ± 63	86.30 ± 1.85	3473 ± 74
	3	17-24	82.96 ± 2.14	3612 ± 76	80.77 ± 2.14	3712 ± 98
14-09-2015	1	1-8	84.18 ± 1.93	3561 ± 82	81.76 ± 2.15	3667 ± 96
	2	9-16	87.00 ± 1.69	3446 ± 67	84.67 ± 1.93	3541 ± 81
	3	17-24	97.14 ± 1.88	3086 ± 60	94.85 ± 2.01	3161 ± 67
15-09-2014	1	1-8	82.55 ± 1.96	3632 ± 86	80.41 ± 2.30	3728 ± 106
	2	9-16	88.08 ± 1.78	3404 ± 69	86.03 ± 1.96	3485 ± 80
	3	17-24	98.04 ± 1.91	3058 ± 59	96.74 ± 2.05	3099 ± 66

These differences in the quality of the data and in the actual execution of the observations must all be taken into account when the data is reduced. In addition to differences in the observations arising from the conditions, there are also differences as a result of the time between the observations. Table 1.3 shows the mean measured resolution and resolving power, at the appropriate rotator angles, for each night where the NGC 55 data were taken. This table shows that the resolution can vary significant between each night, particularly on detector three where the mean resolving power changes by a factor of 1/5. Therefore, this must be taking into consideration when combining exposures on different nights. This is solved by using a simple Gaussian filter (as first described in Chapter ??) to degrade the resolution of the spectra to that of the lowest resolution spectrum within the data set. For example, all spectra for a star in IFU 1 would be degraded to a resolution of 3302 (see Table 1.3) before being combined into a master spectrum for the four nights.

The observations were reduced using the recipes provided by the Software Package

for Astronomical Reduction with KMOS (SPARK; Davies, R. I. et al., 2013). The standard KMOS/esorex routines were used to calibrate and reconstruct the science and standard-star data cubes as outlined by Davies, R. I. et al. (2013) including a correction which corrects for the readout column bias as well as enhancing the bad pixel mask following Turner et al. (in prep.). Using the reconstructed data cubes the pipeline was used to extract science and sky spectra in a consistent way for all exposures.

Sky subtraction was performed using the ESO SKYCORR package (Noll et al., 2014). SKYCORR is an instrument independent tool that applies a scaling to a sky spectrum given a pair of observed and sky spectra in order to more accurately match the sky lines in the observed spectrum and hence, provide a more accurate sky subtraction. This works by adapting the reference sky spectrum to correct for differences as a result of temporal and spatial airglow variability. This software is specifically designed for observations at Cerro Paranal and has been shown to be an effective tool for various different science goals (e.g. Noll et al., 2014; Gazak et al., 2015; Fossati et al., 2016; La Barbera et al., 2016).

Telluric correction is performed on each sky subtracted spectrum (before combination) using the method described in full in Chapter ???. Briefly, additional corrections are made to the standard KMOS/esorex method of telluric correction by correcting for potential offsets between the wavelength solutions of the science and telluric spectra using a iterative cross-correlation approach. In addition, a simple scaling is applied to the telluric spectrum in order to more accurately match the telluric absorption in the science spectrum. Once these addition corrections have been implemented, I divide the science spectrum by the telluric using only the 1.16–1.21  $\mu\text{m}$  region.

As mentioned above, during each night of observing at least one telluric standard-star was observed. Where multiple telluric spectra were available for a single science spectrum, all appropriate telluric spectra were used to apply the telluric correction. The spectra resulting from these corrections are then compared visually and the spectrum producing the fewest residuals is selected. There were instances where multiple spectra were of equal quality, in these cases both spectra were used in the combination process.

To combine the fully calibrated and corrected spectra on each night, I first degrade the spectral resolution of all spectra to the lowest resolution of the set as defined by Table 1.3. Once all spectra are at a constant resolution I

correct for any differences in the wavelength solution by using an iterative cross-correlation approach, where the spectra are all corrected to the rest frame of a single “reference” spectrum. The choice of the reference spectrum is important as if one selected a poor quality reference spectrum with strong sky- or telluric-correction residuals, this could result in an alignment of the residuals which would amplify these features when finally combined. To avoid this, the highest-quality spectrum for each target is selected as the reference spectrum. In practise, this was typically frame four of the night of 16-09-2013.

This procedure mainly corrects for differences in the wavelength solution from different nights. Typically on an individual night (particularly in the case of 14-09-2013 and 16-09-2013) there are not significant differences in the wavelength solution. Once this correction is implemented all spectra are combined using a simple median combine. This simple method is preferred to something more sophisticated as there were significant sky- and telluric-correction residuals present in many of these spectra which are found to be most effectively extinguished using a median combination.

## 1.5 Results and Discussion

### 1.5.1 Radial Velocities

Radial velocities are measured using the method described first in Chapter ?? where radial velocities are measured using several strong spectral features within the 1.16–1.21  $\mu\text{m}$  region. Each of these spectral features is independently used to measure a radial velocity where the value quoted is the average of these measurements and the uncertainties are defined by the standard deviation of the measurements. This method is known to work well on KMOS spectra Lapenna et al. (2015); Patrick et al. (2015, 2016).

Velocities are measured by combining frames from each night individually using the standard KMOS/esorex routines, rather than the method described above. Estimated radial velocities from each KMOS pointing is listed in Table 1.1 alongside the average radial velocity for each target, where any significantly discrepant measurement has been excluded as a result of residuals in the spectrum perturbing the fit (marked by note c in Table 1.1). This is a particular problem on the night of 14-09-2014 where 7/20 velocity measurements were

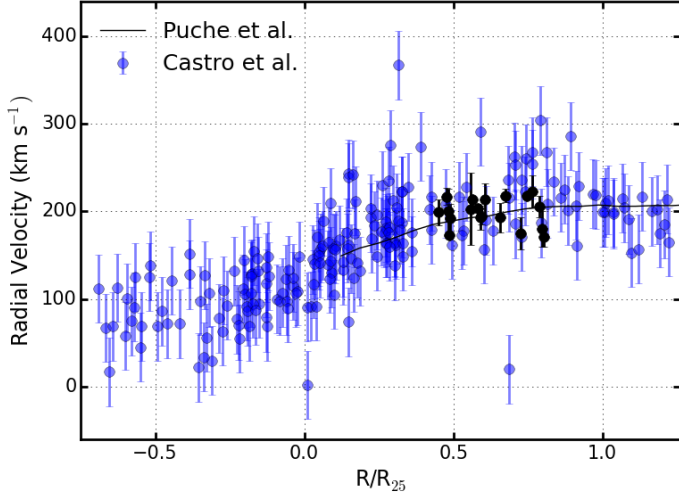


**Figure 1.4** Radial velocities for the KMOS RSGs (black points) shown against projected radius from the centre of NGC 55 as defined by the Two Micron All Sky Survey (2MASS; Skrutskie et al., 2006) scaled by  $R_{25} = 16.2 \pm 0.4$  arcmin (de Vaucouleurs et al., 1991). Blue points show data for  $\sim 200$  BSGs in NGC 55 from Castro et al. (2008); shown with 50% transparency to highlight densely populated areas alongside the rotation curve of NGC 55 (black solid line; Puche, Carignan & Wainscoat, 1991).

excluded. Uncertainties quoted on the average are the standard deviation of the measurements on each night. Three targets (NGC55-RSG22, NGC55-RSG36 and NGC55-RSG60) have been excluded from this average based on their unreliable radial velocity estimates. Given the significant variability in these measurements on each night, an assessment on membership to NGC 55 is impossible given the current data. Therefore, henceforth, these targets are excluded from the sample.

Comparing the estimated velocities to previous measurements we find good agreement with velocities measured for  $\sim 200$  BSGs in NGC 55 in (Castro et al., 2008) as well as with measurements of the velocity from the HI gas (Puche, Carignan & Wainscoat, 1991). The estimated radial velocities as a function of galactocentric distance shown in Figure where previous measurements are also shown for comparison. The radius at which the surface brightness first reaches  $25$  mag/arcsec $^2$  in the  $B$ -band ( $R_{25}$  e.g. Schneider, 2015) is shown for scale ( $R_{25} = 16.2 \pm 0.4$  arcmin de Vaucouleurs et al., 1991). We find no evidence for a systematic offset between the measurements of Castro et al. (2008) and those measured in this study.

As the observed data is taken over four different epochs, the variability of

each source can be assessed. No clear evidence for variability is found for any target within the observed sample. To assess variability, the variability criteria of (Snault-Brunet et al., 2012) is employed, i.e.

$$\left| \frac{RV_i - \mu}{\sigma_i} \right| > 4.0, \quad (1.1)$$

where  $RV_i$  is the radial velocity with an associated uncertainty  $\sigma_i$  measured on an individual night  $i$  and  $\mu$  is the average radial velocity for the target. Using this criteria on all targets finds that no targets show evidence for variability. This adds strength to the suggestion that observed RSGs are intrinsically single objects as a result of the length of time spent as a RSG in a binary is significantly decreased (see discussion in Chapter ??).

### 1.5.2 Stellar Parameters

Stellar parameters are estimated for each target using the  $J$ -band analysis technique detailed in Chapter ???. This analysis is used to measure stellar parameters, including overall metallicity – to a precision of  $\pm 0.15$  dex at the resolution of KMOS observations with  $S/N \geq 100$ . The parameter ranges are given shown in Chapter ??, Table ??.

The analysis uses synthetic RSG spectra, extracted from MARCS model atmospheres (Gustafsson et al., 2008), computed with corrections for non-local thermodynamic equilibrium for lines from titanium, iron, silicon and magnesium (Bergemann et al., 2012, 2013, 2015). The synthetic spectra are compared with observations using the  $\chi^2$ -squared statistic and the synthetic spectra are degraded to the resolution and sampling of the observations.

Estimated stellar parameters are listed in Table 1.4 and the best-fit model spectra are shown with the final reduced science spectra in Figure ???. Assuming no spatial variations in metallicity the average metallicity of the sample is  $-0.36 \pm 0.25$  dex. This average value compares well to the average metallicity measured using 12 BSGs in NGC 55 from (Castro et al., 2012,  $-0.4 \pm 0.13$ ). These authors find no evidence for spatial variations in metallicity in NGC 55, however, recently, Kudritzki et al. (in prep) measure metallicities for  $\sim 60$  BSGs in NGC 55 covering a larger spatial extent and find evidence for a metallicity gradient of xx.xx dex/kpc: the first detected in this galaxy. Using a maximum likelihood

**Table 1.4** Physical parameters determined for the KMOS targets in NGC 55.

Target	IFU	$\xi$ (km s $^{-1}$ )	[Z]	$\log g$	T <sub>eff</sub> (K)	Notes
NGC55-RSG19	6	$4.0 \pm 0.4$	$-0.10 \pm 0.09$	$0.12 \pm 0.10$	$4260 \pm 80$	
NGC55-RSG24	10	$4.2 \pm 0.6$	$-0.43 \pm 0.24$	$-0.37 \pm 0.75$	$4180 \pm 330$	
NGC55-RSG25	8	$3.2 \pm 0.9$	$-0.53 \pm 0.33$	$0.12 \pm 0.36$	$3460 \pm 250$	
NGC55-RSG26	4	$3.2 \pm 0.7$	$-0.64 \pm 0.34$	$0.12 \pm 0.25$	$3560 \pm 280$	
NGC55-RSG35	12	$4.0 \pm 0.6$	$-0.35 \pm 0.26$	$-0.13 \pm 0.24$	$3750 \pm 120$	
NGC55-RSG39	14	$3.3 \pm 0.7$	$-0.28 \pm 0.28$	$-0.13 \pm 0.25$	$3700 \pm 100$	
NGC55-RSG43	24	$3.7 \pm 0.8$	$-0.27 \pm 0.26$	$0.12 \pm 0.98$	$3960 \pm 250$	
NGC55-RSG57	1	$4.0 \pm 0.7$	$-0.39 \pm 0.28$	$0.10 \pm 0.24$	$3550 \pm 270$	
NGC55-RSG58	15	$3.5 \pm 0.7$	$-0.38 \pm 0.27$	$0.12 \pm 0.96$	$3750 \pm 140$	
NGC55-RSG65	17	$4.2 \pm 0.5$	$-0.25 \pm 0.19$	$0.11 \pm 0.97$	$3750 \pm 180$	
NGC55-RSG73	19	$3.2 \pm 0.5$	$-0.26 \pm 0.15$	$-0.86 \pm 0.50$	$3830 \pm 300$	

MCMC parameter estimation for a linear fit to the metallicities measured for RSGs in NGC 55 I find (thus far) no evidence for spatial variations in metallicity, however, this is unsurprising given the spatial coverage and uncertainties associated with the measurements. In order to more accurately assess spatial variations in metallicity one would require a larger sample covering the full spatial profile of NGC 55.

Luminosities have been calculated for the targets using the bolometric corrections of [Maries, B. et al., 2013] where the HST bandpass where available, otherwise the ground-based *I*-band filter has been used. Figure 1.7 shows a H-R diagram for these targets using the temperatures estimated in Section 1.5 along with SMC-like evolutionary tracks (Georgy et al., 2013). Results for 15 RSGs in NGC 300 (a fellow Sculptor galaxy also at  $\sim 1.9$  Mpc) are shown in green on this figure for comparison (Gazak et al., 2015). This appears [Gazak et al., 2015] show a difference in the temperatures of the RSGs in the sample, however, we caution that the uncertainties on the temperatures presented in this study are significantly larger than those in (Gazak et al., 2015).

## 1.6 Conclusions

I have presented multi-epoch near-IR spectroscopic observations of 22 RSGs in the Sculptor Group galaxy NGC 55. Radial velocities are presented and are shown to agree well with previous measurements in this galaxy, where all targets with reliable radial velocity measurements are consistent with membership to NGC 55: confirming their nature as supergiants. Variability is assessed for each target and I find no evidence for variability. A lack of variability is what one would expect from a sample consisting of single stars.

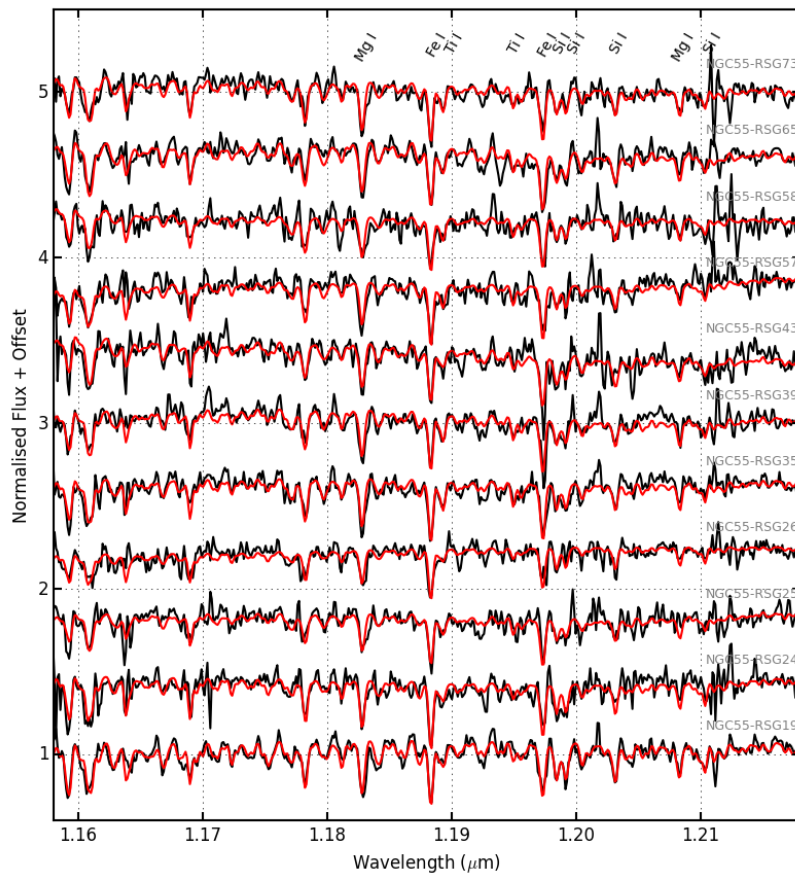


**Figure 1.5** Observed and best-fit model spectra of RSGs in NGC55 (black and red lines, respectively). The lines used for the analysis, from left-to-right by species, are  $Fe\,I\lambda\lambda 1.188285, 1.197305$ ;  $Mg\,I\lambda\lambda 1.182819, 1.208335$ ;  $Si\,I\lambda\lambda 1.198419, 1.199157, 1.203151, 1.210353$ ;  $Ti\,I\lambda\lambda 1.189289, 1.194954$ .

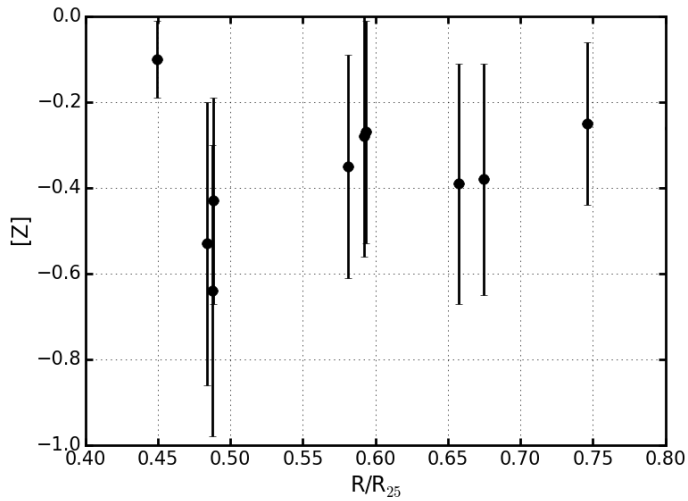


**Figure 1.6** Metalicities for KMOS RSGs (black points) shown against projected radius from the centre of NGC 55 as defined by the Two Micron All Sky Survey (2MASS; Skrutskie et al., 2006) scaled by  $R_{25} = 16.2 \pm 0.4$  arcmin (de Vaucouleurs et al., 1991).

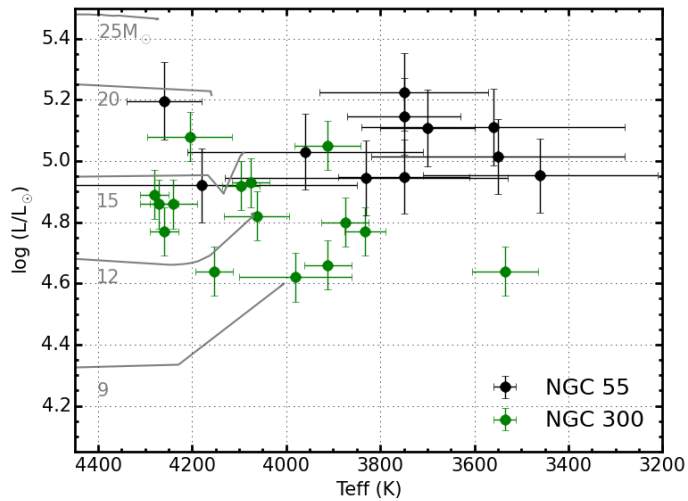


**Figure 1.7** Hertzsprung–Russell diagram for NGC 55. Solid grey lines show SMC-like metallicity evolutionary models including rotation (Georgy et al., 2013). Results from Gazak et al. (2015) in NGC 300 are shown in green for comparison.

Stellar parameters are estimated for 11 of the highest S/N targets in the sample using the *J*-band analysis method described in Chapter ???. The average metallicity of the sample is  $-0.36 \pm 0.25$ , in good agreement with previous results. No evidence is found for spatial variations in metallicity given the present sample, however, we note that this is expected as a result of the combination of the spatial coverage of the sample and the uncertainties in the metallicity parameter. Luminosities are calculated and are compared with RSGs in NGC300 (a fellow Sculptor galaxy at  $\sim 1.9$  Mpc) where there appears to be slight differences in the average effective temperatures of the two samples.

# Chapter 2

## Conclusions

### 2.1 Summary

In this thesis I have used near-IR spectroscopic observations to measure the chemical abundance of RSGs in different environments within the Local Universe. I have detailed the background theory surrounding the evolution of massive stars and their pivotal role in shaping the Universe. In order to make the best use of the extremely luminous nature of RSGs, I have described and detailed KMOS: the only near-IR multi-object spectrograph in the southern hemisphere.

I have developed and tested a grid-based analysis technique to estimate stellar parameters of RSGs using medium-resolution  $J$ -band spectroscopy. I estimate parameters by sampling the posterior probability density function using a maximum-likelihood approach and shown that this technique is not only internally consistent but is also in good agreement with literature measurements.

In Chapter ?? this technique is applied to measure the chemistry and kinematics of a YMC in the LMC: NGC 2100. KMOS spectra of 14 RSGs in NGC 2100 are used to estimate the dynamical properties of this star cluster for the first time. This study demonstrates that KMOS can be used to measure velocities of stars in external galaxies to a precision of  $<5\text{ km s}^{-1}$  and places an upper limit on the line-of-sight velocity dispersion of NGC 2100 at  $\sigma_{1D} = 3.9\text{ km s}^{-1}$ , at the 95% confidence level, where no evidence is found for spatial variations in this estimate. Using this upper limit, an upper limit to the dynamical mass of NGC 2100 has been calculated (assuming virial equilibrium) as  $M_{dyn} = 15.2 \times 10^4 M_\odot$ , in good

agreement with the literature value of the photometric mass for NGC 2100.

The chemistry of NGC 2100 has been estimated using the analysis technique developed in this thesis where the average present-day metallicity of NGC 2100 is  $[Z] = -0.43 \pm 0.10$  dex, which agrees well with previous studies in this cluster and with studies of the young stellar population of the LMC.

The observational properties of the RSGs in NGC 2100 are compared with a star cluster of similar age and mass at Solar-like metallicity. This comparison allows differences in the observational properties of RSGs at different metallicities to be assessed and I show that there appears to be no significant difference between these Solar-like and LMC-like metallicity clusters.

As the RSGs population dominates the infrared light output of a YMC, of a particular age and mass, I combine the RSG spectra to create a simulated integrated-light cluster-spectrum of NGC 2100. Using the same analysis technique I demonstrate that the stellar parameters estimated using integrated-light spectroscopy of YMCs are representative of the average parameters of the RSG population within the cluster.

In Chapter ?? KMOS spectroscopy of 18 RSGs in the dwarf irregular galaxy NGC 6822 is presented. The KMOS data used in this chapter was obtained using KMOS-SV time before this instrument was released to the general community. This chapter represents the first KMOS study of RSGs and forms the base of which all other studies in this area are built from. In order to characterise the performance of the data reduction I have reduced and analysed the data using two different methods of telluric correction: the more time expensive 24-arm telluric correction and the more efficient three-arm telluric correction method. Both methods give consistent results and the 3-arm telluric correction is shown to work as effectively (in most cases). However, we caution, in the low signal-to-noise regime, the 24-arm telluric method will give more reliable results.

Stellar parameters are calculated using two different analysis techniques and are shown to agree well. The present day metallicity of NGC 6822 from RSGs is  $[Z] = -0.55 \pm 0.13$  dex which is consistent with previous measurements of the young stellar population in NGC 6822. The data show evidence for a low-significance abundance gradient within NGC 6822: the first of its kind in a dwarf irregular galaxy. A larger follow-up study is required in order to fully characterise this gradient.

The chemical abundances of the young and old stellar populations are well explained by a simple closed-box chemical evolution model. However, while an interesting result, we note that the closed-box model is unlikely to be a good assumption for this galaxy given its morphology.

The effective temperatures of RSGs are compared in four galaxies using the same analysis technique. These environments span 0.55 dex in metallicity (Solar to SMC) and no evidence is found for a significant variation in temperature with respect to metallicity. This is in contrast with evolutionary models which, for a similar change in metallicity, produces a shift in the temperature of RSGs of up to 450 K. In addition, in this chapter I argue that the observed shift  spectral type of RSGs (defined at optical wavelengths) with respect to metallicity does not imply that the temperatures of RSGs is dependent upon metallicity.

In Chapter 1 multi-epoch KMOS spectroscopy is presented of 22 RSGs in the Sculptor Group galaxy NGC 55. I have measured radial velocities for each epoch which agree well with previous measurements. All targets with reliable velocities are shown to be consistent with membership  NGC 55. In addition I have assessed the  variability of each target and find no evidence for any variable sources, which is consistent with all targets being single objects.

Stellar parameters are estimated for a sub-sample of the highest S/N targets and the average metallicity is found to be  $-0.36 \pm 0.25$  dex, in good agreement with previous results for BSGs. No evidence is found for spatial variations in metallicity given the present sample, however,  note that this is expected as a result of the combination of the spatial coverage of the sample and the uncertainties in the metallicity parameter.

## 2.2 Future Projects

As the topic of this thesis explores many different environments and attempts to relate observations not only to stellar evolution but also to galaxy evolution in general, there are many future projects which build on the present study. One of the key aims of this thesis has been to develop the use of RSGs as chemical abundance probes in external environments. Having demonstrated the effectiveness of RSGs as useful tools to measure chemical abundances in a range of galaxies in low-metallicity environments, I can move  an initial calibration

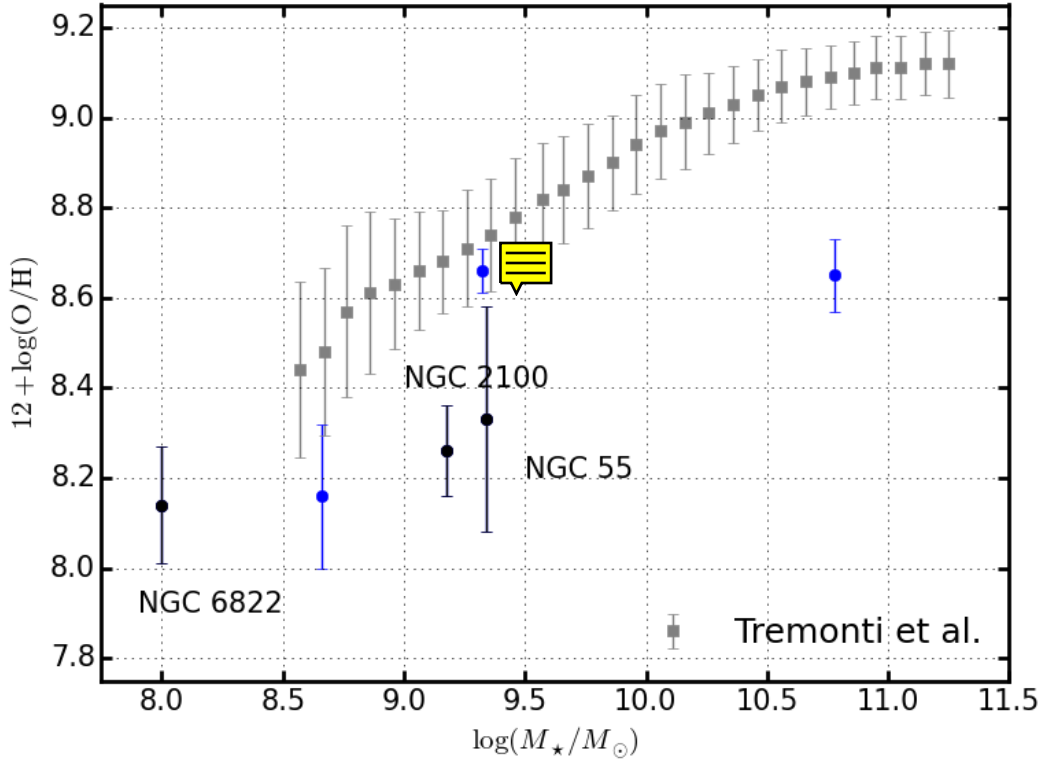


**Figure 2.1** The mass-metallicity relation (MZR) for red supergiant stars (RSGs) in the Local Universe shown with blue points where the work included in this thesis is shown with black points. Metallicity measurements are compiled from the Small Magellanic Cloud (Davies et al., 2015), Perseus OB-1 (Gazak et al., 2014), NGC 300 (Gazak et al., 2015), NGC 2100 (Chapter ??), NGC 6822 (Chapter ??) and NGC 55 (Chapter 1). By introducing the Solar oxygen abundance ratio ( $12 + \log(O/H)_\odot = 8.69$  Asplund et al., 2009) I compare these results to the local MZR for galaxies at  $z \sim 0.1$  (Tremonti et al., 2004). Here [yellow bracket] presents the first results of the MZR as calibrated by RSGs. From this figure it is clear that the absolute measurement of metallicity is significantly overestimated, however, to quantitatively assess this relationship requires a larger sample of RSGs in the Local Universe.

of the MZR using the results presented here.

In Figure 2.1 I present a first-look at the calibration of the MZR in the Local Universe using RSGs as probes of chemical abundances in external galaxies. This figure displays results for six galaxies in the Local Universe (blue points) where three of the metallicity measurements have been made in this thesis (black points). In addition, I show the results of Tremonti et al. (2004) who measured the MZR for  $\sim 50\,000$  SDSS galaxies in the Local Universe ( $z \sim 0.1$ ) and by introducing the Solar oxygen abundance ratio ( $12 + \log (O/H)_\odot = 8.69$  Asplund et al., 2009) I compare these two results. This figure appears to show a significant offset between the metallicity measurements of these two data sets, however, a larger sample of measurements from RSGs is required to quantitatively assess this offset and differences in these relationships.

To solve this problem of poor sample size I am part of a collaboration which aims to measure chemical abundances from RSGs using techniques developed in this study with KMOS observations of RSGs in 13 galaxies. This will allow us to provide a full, independent calibration of the MZR using RSGs in the Local Universe. The observational campaign has been partially successful through use of KMOS GTO and SV data, however, the core proposal for this project was only partially completed in 2015 as a result of poor weather during observing. I am part of the team that has re-applied for time to observe the final three galaxies in this sample. When fully complete, this project will allow for the most precise determination of the MZR to date and will form  basis that all future extragalactic abundance work can be calibrated.

In addition to the calibration of the MZR which was known to be a project which would greater than the work of one PhD thesis, something which was an unexpected result of this thesis has been the result that there exists no significant variation in the temperature of RSGs with respect to metallicity. In Figure 2.2 I compile all observations of RSGs analysed using the same approach as the one described in this thesis. This figure shows effective temperature as a function of the metallicity, estimated using the *J*-band analysis technique, for 81 targets in seven different metallicity environments ranging from super  star in PerOB1 to the low-metallicity environment of NGC 6822 spanning a range of 0.55 dex in metallicity. The mean of the distribution is 3990 K with a standard deviation of 150 K.

From this figure I find no evidence for a temperature variation with respect to

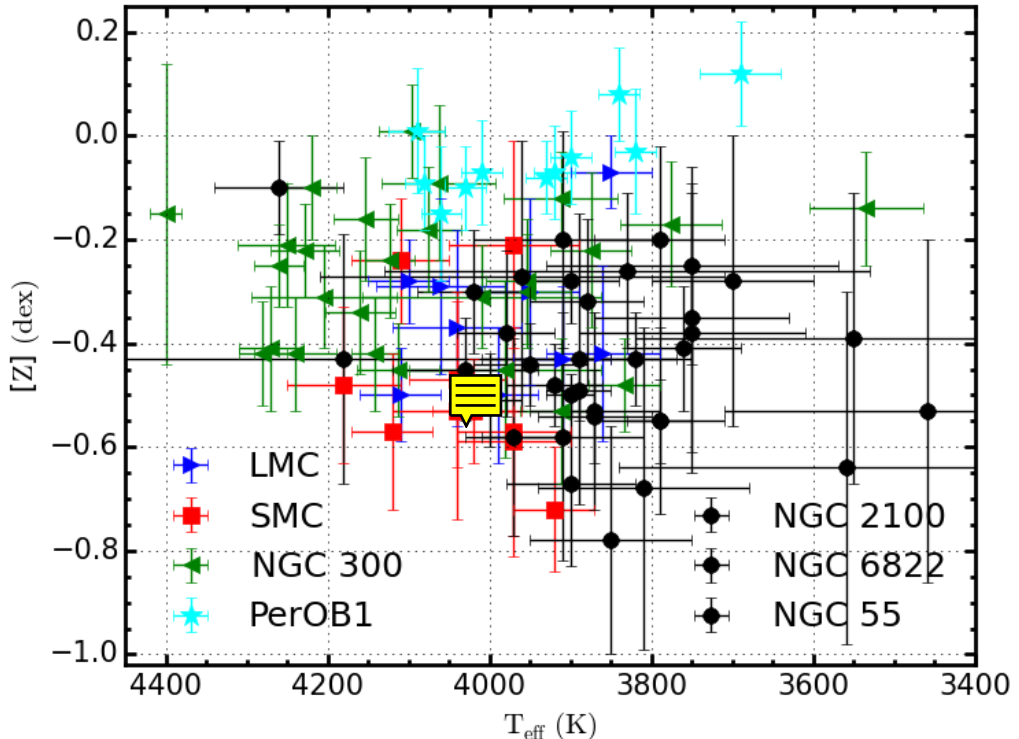


**Figure 2.2** Effective temperatures as a function of metallicity for five different data sets using the *J*-band analysis technique. There appears to be no significant variation in the temperatures of RSGs over a range of 0.55 dex. These results are compiled from the LMC, SMC (blue and red points respectively; Davies et al., 2015), PerOB1 (a Galactic RSG cluster; cyan; Gazak et al., 2014) and NGC 2100 (Chapter ??), NGC 6822 ((Chapter ??)) and NGC 55 ((Chapter 1)). The work included in this thesis is shown with black points.

metallicity. However, to quantify this fully, a larger sample of RSGs must be studied in a range of different metallicity environments. Large spiral galaxies are star-forming environments that typically contain hundreds of RSGs and large spatial variations in abundances. Therefore, a study of a (near) complete population of RSGs in a nearby grand design spiral galaxy e.g. M 3<sub>V</sub>, NGC 300 would be a good starting point to quantitatively assess this interesting result.

In stellar evolutionary models the temperature of RSGs is affected by the choice of the convective mixing length parameter  $\alpha_{MLT}$ , which is usually fixed at the Solar value ( $\alpha = 2.0$ ). A dependence of  $\alpha$  on the metallicity of the star could account for the lack of observed temperatures of RSGs.

In Chapter ?? I present low-significance evidence for a metallicity gradient within NGC 6822. Previously in the literature there have been claims for a weak radial metallicity gradient however these claims have been hampered by a lack of precision in metallicity and/or small sample size. By targeting all candidate RSGs within NGC 6822 using KMOS GTO in April 2016 I will measure metallicities for  $\sim 60$  RSG candidates across the full spatial extent of NGC 6822 (see Chapter ??, Figure ??). These follow-up observations will allow me to definitively quantify the spatial distribution of metallicity within NGC 6822. This is an important result to quantify as a radial metallicity gradient would be direct evidence for a disk structure w<sub>NGC 6822</sub>.

In addition to follow-up spectroscopy in NGC 6822, our collaboration has resubmitted for KMOS spectroscopy of an additional one field in NGC 55 to extend the spatial profile covered in this galaxy. By estimating metallicities for an additional  $\sim 20$  targets in the disk of NGC 55 I will be able to more rigorously quantify the abundance gradient in this galaxy with the aim to independently calibrate the metallicity gradient measured from BSGs (Kudritzki et al. in prep.). In addition to this, by measuring temperatures of the RSGs more accurately in NGC 55 I will be able to quantify the potential offset in temperatures between this data set and that of NGC 300.

In Chapter ?? I presented the first determination of (an upper limit to) the dynamical mass of NGC 2100 as well the unresolved line-of-sight velocity dispersion for this cluster. By obtaining higher resolution spectroscopy of a large sample of stars within this star cluster one could measure the velocity dispersion profile and resolve the line-of-sight velocity dispersion in this cluster. One of my unanswered questions from the study presented in Chapter ?? is: will this

star cluster survive  dissolve in the future? By more accurately determining the mass and velocity dispersion profile of this cluster, this question could be resolved.

In addition to these areas of study mentioned above, I am also interested in further developing the analysis technique presented in Chapter ???. Studies in this area may include fitting for the  $[\alpha/\text{Fe}]$  parameter (rather assuming Solar-like values), an important indicator of stellar evolution and in particular how this parameter depends upon metallicity. Expanding the wavelength range used to estimate stellar parameters and including updated line lists would allow one to estimate individual elemental abundances as well as overall metallicity. A potentially promising channel in this respect is the  $\sim 1.0 \mu\text{m}$  region.

Another interesting avenue to explore with this analysis technique would be to expand the parameter space of the model grid to apply this technique to other mass coars e.g. Cepheid variables and red giant stars.

Finally, great progress has been made in recent years using tools which aid the data reduction process in the near-IR e.g. MOLECFIT, SKYCORR. As near-IR spectroscopy becomes more important in our understanding of astrophysics, these tools will become increasingly relied upon to provide accurate and precise correction In this thesis I have taken the first steps using SKYCORR on KMOS data, where this tool has had great success above what can be achieved neglecting this advanced procedure. In the future I will supplement this by using MOLECFIT to perform telluric correction with the goal of optimising future observing strategies.

## 2.3 Closing Remarks

...over a pint I think!



# Bibliography

- Asplund M., Grevesse N., Sauval A. J., Scott P., 2009, ARA&A, 47, 481
- Bergemann M., Kudritzki R.-P., Gazak Z., Davies B., Plez B., 2015, ApJ, 804, 113
- Bergemann M., Kudritzki R.-P., Plez B., Davies B., Lind K., Gazak Z., 2012, ApJ, 751, 156
- Bergemann M., Kudritzki R.-P., Würl M., Plez B., Davies B., Gazak Z., 2013, ApJ, 764, 115
- Castro N. et al., 2008, A&A, 485, 41
- Castro N. et al., 2012, A&A, 542, A79
- Dalcanton J. J. et al., 2009, ApJS, 183, 67
- Davidge T. J., 2005, ApJ, 622, 279
- Davies B., Kudritzki R.-P., Gazak Z., Plez B., Bergemann M., Evans C., Patrick L., 2015, ApJ, 806, 21
- Davies, B. et al., 2013, ApJ, 767, 3
- Davies, R. I. et al., 2013, A&A, 558, A56
- de Vaucouleurs G., 1961, ApJ, 133, 405
- de Vaucouleurs G., de Vaucouleurs A., Corwin, Jr. H. G., Buta R. J., Paturel G., Fouqué P., 1991, Third Reference Catalogue of Bright Galaxies. Volume I: Explanations and references. Volume II: Data for galaxies between  $0^h$  and  $12^h$ . Volume III: Data for galaxies between  $12^h$  and  $24^h$ .
- Engelbracht C. W. et al., 2004, ApJS, 154, 248
- Ferguson A. M. N., Wyse R. F. G., Gallagher J. S., 1996, AJ, 112, 2567
- Fossati M., Fumagalli M., Boselli A., Gavazzi G., Sun M., Wilman D. J., 2016, MNRAS, 455, 2028
- Gazak J. Z., Davies B., Kudritzki R., Bergemann M., Plez B., 2014, ApJ, 788, 58

- Gazak J. Z. et al., 2015, ApJ, 805, 182
- Georgy C. et al., 2013, A&A, 558, A103
- Gieren W. et al., 2005, The Messenger, 121, 23
- Gieren W., Pietrzyński G., Soszyński I., Bresolin F., Kudritzki R.-P., Storm J., Minniti D., 2008, ApJ, 672, 266
- Gustafsson B., Edvardsson B., Eriksson K., J rgensen U. G., Nordlund Å., Plez B., 2008, A&A, 486, 951
- Hénault-Brunet V. et al., 2012, A&A, 546, A73
- Houk N., 1978, Michigan catalogue of two-dimensional spectral types for the HD stars
- Houk N., Smith-Moore M., 1988, Michigan Catalogue of Two-dimensional Spectral Types for the HD Stars. Volume 4, Declinations -26deg.0to – 12deg.0.
- Hummel E., Dettmar R.-J., Wielebinski R., 1986, A&A, 166, 97
- Karachentsev I. D. et al., 2003, A&A, 404, 93
- La Barbera F., Vazdekis A., Ferreras I., Pasquali A., Cappellari M., Martín-Navarro I., Schönebeck F., Falcón-Barroso J., 2016, MNRAS, 457, 1468
- Lapenna E., Origlia L., Mucciarelli A., Lanzoni B., Ferraro F. R., Dalessandro E., Valenti E., Cirasuolo M., 2015, ApJ, 798, 23
- Nikolaev S., Weinberg M. D., 2000, ApJ, 542, 804
- Noll S., Kausch W., Kimeswenger S., Barden M., Jones A. M., Modigliani A., Szyszka C., Taylor J., 2014, A&A, 567, A25
- Patrick L. R., Evans C. J., Davies B., Kudritzki R., Hénault-Brunet V., Bastian N., Lapenna E., Bergemann M., 2016, ArXiv e-prints
- Patrick L. R., Evans C. J., Davies B., Kudritzki R.-P., Gazak J. Z., Bergemann M., Plez B., Ferguson A. M. N., 2015, ApJ, 803, 14
- Pietrzyński G. et al., 2006, AJ, 132, 2556
- Pritchett C. J., Schade D., Richer H. B., Crabtree D., Yee H. K. C., 1987, ApJ, 323, 79
- Puche D., Carignan C., Wainscoat R. J., 1991, AJ, 101, 447
- Robinson B. J., van Damme K. J., 1964, in IAU Symposium, Vol. 20, The Galaxy and the Magellanic Clouds, Kerr F. J., ed., p. 276
- Schneider P., 2015, Extragalactic Astronomy and Cosmology: An Introduction

- Skrutskie M. F. et al., 2006, AJ, 131, 1163
- Tremonti C. A. et al., 2004, ApJ, 613, 898
- van de Steene G. C., Jacoby G. H., Praet C., Ciardullo R., Dejonghe H., 2006, A&A, 455, 891
- Webster B. L., Smith M. G., 1983, MNRAS, 204, 743
- Westmeier T., Koribalski B. S., Braun R., 2013, MNRAS, 434, 3511